

1 On the relationship between the mesospheric sodium layer and the meteoric input function

2 Yanlin Li¹, Tai-Yin Huang², Julio Urbina¹, Fabio Vargas³, Wuhu Feng⁴

3 1. Department of Electrical Engineering, Pennsylvania State University, University Park, PA, USA

4 2. Department of Physics, Penn State Lehigh Valley, Center Valley, PA, USA

5 3. Department of Electrical Engineering, University of Illinois Urbana-Champaign, Champaign, IL, USA

6 4. National Centre for Atmospheric Science, University of Leeds, Leeds, UK

7 *Correspondence to:* Tai-Yin Huang (tuh4@psu.edu)

8

9

10 Abstract

11

12 This study examines the relationship between the concentration of atmospheric sodium and its
13 Meteoric Input Function (MIF). We use the measurements from the Colorado State University (CSU)
14 Lidar and the Andes Lidar Observatory (ALO) with a new numerical model that includes sodium
15 chemistry in the mesosphere and lower thermosphere (MLT) region. The model is based on the
16 continuity equation to treat all sodium-bearing species and runs at a high temporal resolution. The
17 model simulation employs data assimilation to compare the MIF inferred from the **meteor radiant**
18 **distribution** and the MIF derived from the new sodium chemistry model. The simulation captures the
19 seasonal variability of sodium number density compared with lidar observations over the CSU site.
20 However, there were discrepancies for the ALO site, which is close to the South Atlantic Anomaly (SAA)
21 region, indicating it is challenging for the model to capture the observed sodium over ALO. The CSU site
22 had significantly more lidar observations (27,930 hours) than the ALO sites (1872 hours). The simulation
23 revealed that the uptake of the sodium species on meteoric smoke particles was a critical factor in
24 determining the sodium concentration in MLT, with the sodium removal rate by uptake found to be
25 approximately three times that of the NaHCO₃ dimerization. Overall, the study's findings provide
26 valuable information on the correlation between MIF and sodium concentration in the MLT region,
27 contributing to a better understanding of the complex dynamics in this region. This knowledge can
28 inform future research and guide the development of more accurate models to enhance our
29 comprehension of the MLT region's behavior.

30

31 **Keywords:** Sodium layer, sodium chemistry, Meteor radiant distribution, Meteoroid input function

32

33 Key points:

34

- 35 ● A high-time resolution, time-dependent Na chemistry model is developed.
- 36 ● Ablated global meteoroid material inputs inferred from ALO and CSU observations are about **83**
37 **t d⁻¹** and **53 t d⁻¹**, respectively.
- 38 ● **The frequency of meteor occurrences might not provide a precise reflection of the mass of**
39 **meteoroid material input.**

39

40

41 1. Introduction

42 Micro-meteoroids enter the Earth's atmosphere day and night, depositing their constituents into the
43 atmosphere via ablation, creating a region that hosts various metal species, for example, Fe, K, Si, Mg,
44 Ca, and Na, in both neutral and ion form (Plane et al., 2015; Plane et al., 2021; and references therein).
45 The region is commonly referred to as the mesosphere and lower thermosphere (MLT), located between
46 75 and 110 km altitude. The metal layers in the MLT often serve as the tracers that facilitate the
47 investigation of the dynamical and chemical processes within the region (Takahashi et al., 2014; Qiu et
48 al., 2021). Quantitative measurements of metal atoms have been made since the 1950s (Hunten, 1967)
49 through a variety of ground or space-borne technologies (Koch et al., 2021; Koch et al., 2022). The large
50 resonant scattering cross-section (Bowman et al., 1969) and the substantial presence of the sodium
51 atom in the MLT make it one of the most researched metal layers in the atmosphere (Yu et al., 2022).

52 The sodium layer is usually studied via observations carried out by resonance lidars, satellites, and
53 through Na D-line emission at 589.0nm and 589.6nm (Plane, 2010; Plane et al., 2012; Hedin and
54 Gumbel, 2011; Langowski et al., 2017; Andrioli et al., 2019; Li et al., 2020a). The sodium vertical profiles
55 retrieved by lidars have been commonly used as a tracer to study atmospheric dynamics, e.g., gravity
56 waves, wind shear, etc. The long-term seasonal and short-term diurnal variability of metallic species
57 have been investigated by several studies (Feng et al., 2013; Marsh et al., 2013; Cai et al., 2019a, b; Yu et
58 al., 2022). A typical sodium chemistry scheme consists of neutral chemistry, ion chemistry, and
59 photolysis. The sodium chemistry research in recent years has primarily been based on the sodium
60 chemistry model by Plane (2004), which has been cited in various subsequent works, including Bag et al.
61 (2015) and references therein.

62 As meteoroids are the primary source of metal layers in the atmosphere, including the sodium layer,
63 the Meteoroid Input Function (MIF) plays a crucial role in the modeling of metallic layers in the
64 atmosphere. The MIF is a function designed to comprehend the impact of the temporal and spatial
65 variability of the meteoroid on the atmosphere (Pifko et al., 2013). Sporadic meteors are estimated to
66 make up more than 95% of the total meteoroid population by comparing the number of meteors
67 originating in sporadic sources to those originating in known shower meteor sources (Chau and Galindo,
68 2008). This highlights the importance of incorporating sporadic meteor data in the MIF to accurately
69 understand sodium concentration in the mesosphere and lower thermosphere (MLT) region and its
70 correlation with meteoroid material input. It is well established that there are six apparent sources of
71 sporadic meteors, namely North and South Apex (NA and SA); North and South Toroidal (NT and ST);
72 and Helion and Anti-Helion sources (H and AH) (Campbell-Brown, 2008; Kero et al., 2012; Li et al., 2022).
73 However, the relative strength of these meteor radiant sources varies among the studies. For example,
74 the NA and SA sources are found to be much stronger than other sources in results obtained with High
75 Power Large Aperture (HPLA) radars (Chau et al., 2007; Kero et al., 2012; Li and Zhou, 2019), while
76 specular meteor radars found the difference to be much smaller (Campbell-Brown and Jones, 2005;
77 Campbell-Brown, 2008). The detection sensitivity varies significantly among different facilities. For
78 instance, the Arecibo Observatory (AO) at 18° N, 66° W detects approximately 20 times more meteors
79 per unit area per unit time than the Jicamarca Radio Observatory (JRO) at 12° S, 77° W, and at least 800
80 times more meteors than the Resolute Bay Incoherent Scatter North (RISR-N) radar at 75° N, 95° W,
81 despite all being HPLA facilities (Li et al., 2020, 2023a; Hedges et al., 2022) Of note, meteor flux varies
82 with time and latitude, but the variations cannot account for such a large difference.

83 **Consequently, the total mass of the meteors that enter the Earth's atmosphere is subject to significant**
84 **uncertainties.** In the existing Whole Atmosphere Community Climate Model-Na (WACCM-Na) global
85 sodium model (Dunker et al., 2015), the meteor input function was modeled by placing a flux curve on
86 each radiant meteor source with a definite ratio (more details can be found in Marsh et al., 2013). The
87 flux curve model is based on observations carried out exclusively by the Arecibo Observatory. Although
88 the model can reproduce some of the flux characteristics of the meteors observed at Arecibo, it is a
89 relatively simple model and therefore has several limitations (Li et al., 2022). One of the limitations is
90 that the model cannot reproduce the velocity distribution of the meteors in observations.

91 This study introduces a new numerical model for sodium chemistry that utilizes the continuity equations
92 for all Na-related reactions without steady-state approximations. The main objective is to investigate the
93 relationship between the apparent sodium concentration and the Meteoroid Input Function (MIF) in the
94 MLT region. We then compare the results of the new model with measurements from two lidar
95 instruments, namely the Colorado State University (CSU) and the Andes Lidar Observatory (ALO).
96 **Furthermore, we compared the MIF derived from the new sodium chemistry model and lidar**
97 **measurements from CSU and ALO, against the results of the high-resolution meteor radiant distribution**
98 **recently deduced from observations conducted at AO.** Finally, we discuss the implications of these
99 comparisons and suggest possible explanations for the observed discrepancy between the MIF derived
100 from radar and those obtained from lidar observations.

101

102 **2. The sodium chemistry model (NaChem)**

103 **2.1 Sodium chemistry**

104 Numerical airglow models have been extensively used to investigate atmospheric airglow chemistry and
105 gravity waves (Huang and Hickey, 2008; Huang and Richard, 2014; Huang, 2015). A new numerical
106 sodium chemistry model, hereafter referred to as NaChem, was developed for this study. Table 1 lists
107 the complete reactions and their corresponding rate coefficients used in NaChem, which includes
108 neutral chemistry, ion chemistry, and photochemistry. The dimerization reaction of NaHCO_3 (reaction 25
109 in Table 1) is the outlet that removes Na atoms in the chemistry scheme. The Na atoms can also be
110 removed by the uptake of sodium species onto meteoric smoke particles (Hunten et al., 1980;
111 Kalashnikova et al., 2000; Plane, 2004), a process that can be turned on or off in the model. This study
112 estimates the MIF in the numerical model by matching the dimerization reaction to maintain the
113 observed sodium present in the MLT. Throughout the rest of the paper, the MIF estimated from the
114 sodium chemistry numerical model will be referred to as MIF(s). On the other hand, the MIF derived
115 from meteor radiant distribution will be referred to as MIF(m). **MIF is a function of time and represents**
116 **the mass of meteoroid material entering Earth's atmosphere.** The MIF(m) is determined through a 3-D
117 meteoroid orbital simulation based on the meteor radiant distribution.

118 The numerical model utilizes the continuity equation to track the time evolution of all 14 Na-related
119 species. Table 2 presents a comprehensive list of these species, along with their corresponding
120 production and loss rates. The background major gas species, including O_3 , O_2 , O, H, H_2 , H_2O , etc., and
121 the temperature are provided by WACCM. Here we use the dynamic version of WACCM nudged with
122 NASA's Modern Era Retrospective Analysis for Research and Application MERRA2 reanalysis data set
123 (Hunziker & Wendt, 1974; Molod et al., 2015; Gettelman et al., 2019). The WACCM reference profiles

124 are linearly interpolated to a resolution of one minute and updated every minute during the simulation.
125 It is worth noting that the Na-related reactions, which are illustrated in Table 2, do not significantly
126 impact the background gas species, as the effect is orders of magnitude smaller than the variation of the
127 major gas species themselves. Therefore, the major gas species are simulated independently of Na-
128 related reactions.

129 **2.2 Numerical scheme**

130 As discussed earlier, it is worth noting that the reactions of sodium chemistry in NaChem share
131 similarities with those in previous models (e.g., Plane et al., 2015 and references therein); however, the
132 implementation of the numerical chemistry scheme differs. NaChem uses continuity equations to treat
133 all chemicals involved, including short-lived intermediate species. Treating all species with the continuity
134 equation is a more straightforward yet accurate approach than using steady-state approximations.
135 Moreover, by treating all species in a uniform procedure, the numerical model is more compact and
136 easier to interpret. The computational capability of a personal computer nowadays has advanced
137 enough to process an ultra-fine time step (microseconds) that is necessary for numerical simulations of
138 short-lived species in a reasonable duration. Still, the differential equations for production and loss of
139 short-lived species can be numerically unstable unless microsecond or even sub-microsecond time step
140 is used (Higham, 2002). The concern of the differential equation instability can be largely mitigated by a
141 first-order exponential integrator (Hochbruck and Ostermann, 2010), i.e.,

142

$$c = x_0 - \frac{a_0}{b_0}$$
$$x_1 = \frac{a_0}{b_0} + ce^{-b_0\Delta t} \tag{1}$$

143

144 Where x_0 is the value of the current step, a_0 is the production of the species, b_0 is the loss of the
145 species, Δt is the step size in time, and x_1 is the value of the next step.

146 The exponential integrator, as expressed in Equation (1), is the solution to the continuity equation.
147 Notably, reaction 25 listed in Table 1 is an exception, which was carried out using explicit Euler
148 integrator in the simulation. This reaction's continuity equation is structured differently from the others
149 because it represents the only mechanism for removing Na atoms from the chemistry simulation, apart
150 from the uptakes of sodium species. Our testing indicates that both the exponential integrator and
151 explicit Euler integrator yield nearly identical results. However, for numerical stability, the explicit Euler
152 integrator requires a step size of $\sim 1\mu\text{s}$, which is orders of magnitude smaller than the exponential
153 integrator. The default time step of NaChem is 0.1 seconds with the exponential integrator.

154

155

156
157
158
159
160

Table 1. Reactions in NaChem. f_a and f_x are branching ratios.

	Reaction	Rate Coefficient	reference
neutral chemistry			
1	$\text{Na} + \text{O}_3 \rightarrow \text{NaO(A)} + \text{O}_2$	$K_1 = 1.1 \times 10^{-9} \exp(-116/T)$	1
2	$\text{NaO(A)} + \text{O} \rightarrow \text{Na}^{(2)\text{P}} + \text{O}_2$	$K_2 = 2.2 \times 10^{-10} (T/200)^{0.5}$, $f_A = 0.14 \pm 0.4$	1,3
3	$\text{NaO(A)} + \text{O} \rightarrow \text{Na}^{(2)\text{S}} + \text{O}_2$	$K_3 = 2.2 \times 10^{-10} (T/200)^{0.5}$, $(1-f_A)$	1,3
4	$\text{NaO(A)} + \text{O}_2 \rightarrow \text{NaO(X)} + \text{O}_2$	$K_4 = 1 \times 10^{-11}$	1
5	$\text{Na} + \text{O}_2 + \text{M} \rightarrow \text{NaO}_2 + \text{M}$	$K_5 = 5.0 \times 10^{-30} (200/T)^{1.22}$	1
6	$\text{NaO}_2 + \text{O} \rightarrow \text{NaO(X)} + \text{O}_2$	$K_6 = 5 \times 10^{-10} \exp(-940/T)$	1
7	$\text{NaO(X)} + \text{O} \rightarrow \text{Na}^{(2)\text{P}} + \text{O}_2$	$K_7 = 2.2 \times 10^{-10} (T/200)^{0.5}$, $f_x = 0.167$	1,2
8	$\text{NaO(X)} + \text{O} \rightarrow \text{Na}^{(2)\text{S}} + \text{O}_2$	$k_8 = 2.2 \times 10^{-10} (T/200)^{0.5}$, $(1-f_x)$	1,2
9	$\text{NaO(X)} + \text{O}_3 \rightarrow \text{NaO}_2 + \text{O}_2$	$k_9 = 1.1 \times 10^{-9} \exp(-568/T)$	1
10	$\text{NaO(X)} + \text{O}_3 \rightarrow \text{Na} + 2\text{O}_2$	$k_{10} = 3.2 \times 10^{-10} \exp(-550/T)$	1
11	$\text{NaO(X)} + \text{O}_2 + \text{M} \rightarrow \text{NaO}_3 + \text{M}$	$k_{11} = 5.3 \times 10^{-30} (200/T)$	1
12	$\text{NaO(X)} + \text{H} \rightarrow \text{Na} + \text{OH}$	$k_{12} = 4.4 \times 10^{-10} \exp(-668/T)$	1
13	$\text{NaO(X)} + \text{H}_2 \rightarrow \text{NaOH} + \text{H}$	$k_{13} = 1.1 \times 10^{-9} \exp(-1100/T)$	1
14	$\text{NaO(X)} + \text{H}_2 \rightarrow \text{Na} + \text{H}_2\text{O}$	$k_{14} = 1.1 \times 10^{-9} \exp(-1400/T)$	1
15	$\text{NaO(X)} + \text{H}_2\text{O} \rightarrow \text{NaOH} + \text{OH}$	$k_{15} = 4.4 \times 10^{-10} \exp(-507/T)$	1
16	$\text{NaO(X)} + \text{CO}_2 + \text{M} \rightarrow \text{NaCO}_3 + \text{M}$	$K_{16} = 1.3 \times 10^{-27} (200/T)$	1
17	$\text{NaO}_2 + \text{H} \rightarrow \text{Na} + \text{HO}_2$	$K_{17} = 1.0 \times 10^{-9} \exp(-1000/T)$	1
18	$\text{NaO}_3 + \text{O} \rightarrow \text{Na} + 2\text{O}_2$	$k_{18} = 2.5 \times 10^{-10} (T/200)^{0.5}$	1
19	$\text{NaCO}_3 + \text{O} \rightarrow \text{NaO}_2 + \text{CO}_2$	$k_{19} = 5.0 \times 10^{-10} \exp(-1200/T)$	1
20	$\text{NaCO}_3 + \text{H} \rightarrow \text{NaOH} + \text{CO}_2$	$k_{20} = 1.0 \times 10^{-9} \exp(-1400/T)$	1
21	$\text{NaOH} + \text{H} \rightarrow \text{Na} + \text{H}_2\text{O}$	$k_{21} = 4.0 \times 10^{-11} \exp(-550/T)$	1
22	$\text{NaOH} + \text{CO}_2 + \text{M} \rightarrow \text{NaHCO}_3 + \text{M}$	$k_{22} = 1.9 \times 10^{-28} (200/T)^1$	1
23	$\text{NaHCO}_3 + \text{H} \rightarrow \text{Na} + \text{H}_2\text{O} + \text{CO}_2$	$k_{23} = 1.1 \times 10^{-11} \exp(-910/T)$	1
24	$\text{NaHCO}_3 + \text{H} \rightarrow \text{Na} + \text{H}_2\text{CO}_3$	$k_{24} = 1.84 \times 10^{-13} T^{0.777} \exp(-1014/T)$	1
25	$2\text{NaHCO}_3 + \text{M} \rightarrow (\text{NaHCO}_3)_2 + \text{M}$	$k_{25} = 8.8 \times 10^{-10} \exp(T/200)^{-0.23}$	1
26	$\text{Na}^{(2)\text{P}} \rightarrow \text{Na}^{(2)\text{S}} + h\nu(589.0-589.6 \text{ nm})$	$K_{26} = 6.26 \times 10^7$	1
ion-molecule chemistry			
27	$\text{Na} + \text{O}_2^+ \rightarrow \text{Na}^+ + \text{O}_2$	$K_{27} = 2.7 \times 10^{-9}$	1
28	$\text{Na} + \text{NO}^+ \rightarrow \text{Na}^+ + \text{NO}$	$K_{28} = 8.0 \times 10^{-10}$	1
29	$\text{Na}^+ + \text{N}_2 + \text{M} \rightarrow \text{NaN}_2^+ + \text{M}$	$k_{29} = 4.8 \times 10^{-30} (T/200)^{-2.2}$	1
30	$\text{Na}^+ + \text{CO}_2 + \text{M} \rightarrow \text{NaCO}_2^+ + \text{M}$	$k_{30} = 3.7 \times 10^{-29} (T/200)^{-2.9}$	1
31	$\text{NaN}_2^+ + \text{O} \rightarrow \text{NaO}^+ + \text{N}_2$	$k_{31} = 4.0 \times 10^{-10}$	1
32	$\text{NaO}^+ + \text{N}_2 \rightarrow \text{NaN}_2^+ + \text{O}$	$k_{32} = 1.0 \times 10^{-12}$	1
33	$\text{NaO}^+ + \text{O} \rightarrow \text{Na}^+ + \text{O}_2$	$k_{33} = 1.0 \times 10^{-11}$	1
34	$\text{NaO}^+ + \text{O}_2 \rightarrow \text{Na}^+ + \text{O}_3$	$k_{34} = 5.0 \times 10^{-12}$	1
35	$\text{NaN}_2^+ + \text{X} \rightarrow \text{NaX}^+ + \text{N}_2$ ($\text{X}=\text{CO}_2, \text{H}_2\text{O}$)	$k_{35} = 6.0 \times 10^{-10}$	1
36	$\text{NaY}^+ + \text{e} \rightarrow \text{Na} + \text{Y}$ ($\text{Y}=\text{N}_2, \text{CO}_2, \text{H}_2\text{O}, \text{O}$)	$k_{36} = 1.0 \times 10^{-6} (T/200)^{-0.5}$	1
photochemical reactions			
37	$\text{NaO(A)}/\text{NaO(X)} + h\nu \rightarrow \text{Na} + \text{O}$	$K_{37} = 5.5 \times 10^{-2}$	1

38	$\text{NaO}_2 + \text{h}\nu \rightarrow \text{Na} + \text{O}_2$	$K_{38} = 1.9 \times 10^{-2}$	1
39	$\text{NaOH} + \text{h}\nu \rightarrow \text{Na} + \text{OH}$	$K_{39} = 1.8 \times 10^{-2}$	1
40	$\text{NaHCO}_3 + \text{h}\nu \rightarrow \text{Na} + \text{HCO}_3$	$K_{40} = 1.3 \times 10^{-4}$	1
41	$\text{Na} + \text{h}\nu \rightarrow \text{Na}^+ + \text{e}^-$	$K_{41} = 2 \times 10^{-5}$	1

161 *1:Plane (2004), 2: Plane (2012), 3: Griffin et al. (2001).

162

163 Table 2. The production and loss terms of the sodium-related species.

	Species	Prod	Loss
a1	Na(2P)	$k_2[\text{a}_3][\text{O}] + k_7[\text{a}_5][\text{O}];$	1*
a2	Na	$k_3[\text{a}_3][\text{O}] + k_8[\text{a}_5][\text{O}] + k_{10}[\text{a}_5][\text{O}_3] + k_{12}[\text{a}_5][\text{H}] + k_{14}[\text{a}_5][\text{H}_2] + k_{17}[\text{a}_4][\text{H}] + k_{18}[\text{a}_6][\text{O}] + k_{21}[\text{a}_7][\text{H}] + k_{23}[\text{a}_9][\text{H}] + k_{24}[\text{a}_9][\text{H}] + k_{36}[\text{a}_{11}][\text{e}] + k_{36}[\text{a}_{13}][\text{e}] + k_{36}[\text{a}_{12}][\text{e}] + k_{36}[\text{a}_{14}][\text{e}] + [\text{a}_1] + k_{37}[\text{a}_3][\text{h}\nu] + k_{37}[\text{a}_5][\text{h}\nu] + k_{38}[\text{h}\nu][\text{a}_4] + k_{39}[\text{h}\nu][\text{a}_7] + k_{40}[\text{h}\nu][\text{a}_9];$	$k_1[\text{O}_3] + k_5[\text{O}_3] + k_5[\text{O}_2][\text{M}] + k_{27}[\text{O}_2^+] + k_{28}[\text{NO}^+] + k_{41}[\text{h}\nu];$
a3	NaO(A)	$k_1[\text{a}_2][\text{O}_3]$	$k_2[\text{O}] + k_3[\text{O}] + k_4[\text{O}_2] + k_{37}[\text{h}\nu]$
a4	NaO ₂	$k_5[\text{a}_2][\text{O}_2][\text{M}] + k_9[\text{a}_5][\text{O}_3] + k_{19}[\text{a}_8][\text{O}]$	$k_6[\text{O}] + k_{17}[\text{H}] + k_{38}[\text{h}\nu]$
a5	NaO(X)	$k_5[\text{a}][\text{O}_3] + k_4[\text{a}_3][\text{O}_2] + k_6[\text{a}_4][\text{O}]$	$k_7[\text{O}] + k_8[\text{O}] + k_9[\text{O}_3] + k_{10}[\text{O}_3] + k_{11}[\text{O}_2][\text{M}] + k_{12}[\text{H}] + k_{13}[\text{H}_2] + k_{14}[\text{H}_2] + k_{15}[\text{H}_2\text{O}] + k_{16}[\text{CO}_2][\text{M}] + k_{37}[\text{h}\nu]$
a6	NaO ₃	$k_{11}[\text{a}_5][\text{O}_2][\text{M}]$	$k_{18}[\text{O}]$
a7	NaOH	$k_{13}[\text{a}_5][\text{H}_2] + k_{15}[\text{a}_5][\text{H}_2\text{O}] + k_{20}[\text{a}_8][\text{H}]$	$k_{21}[\text{H}] + k_{22}[\text{CO}_2][\text{M}] + k_{39}[\text{h}\nu]$
a8	NaCO ₃	$k_{16}[\text{a}_5][\text{CO}][\text{M}]$	$k_{19}[\text{O}] + k_{20}[\text{H}]$
a9	NaHCO ₃	$k_{22}[\text{a}_7][\text{CO}_2][\text{M}]$	$k_{23}[\text{H}] + k_{24}[\text{H}] + 2k_{25}[\text{a}_9][\text{M}] + k_{40}[\text{h}\nu]$
a10	Na ⁺	$k_{27}[\text{a}_2][\text{O}_2^+] + k_{28}[\text{a}_2][\text{NO}^+] + k_{33}[\text{a}_{13}][\text{O}] + k_{34}[\text{a}_{13}][\text{O}_2] + k_{41}[\text{h}\nu][\text{a}_2]$	$k_{29}[\text{N}_2][\text{M}] + k_{30}[\text{CO}_2][\text{M}]$
a11	NaN ₂ ⁺	$k_{29}[\text{a}_{10}][\text{N}_2][\text{M}] + k_{32}[\text{a}_{13}][\text{N}_2]$	$k_{31}[\text{O}] + k_{35}[\text{CO}_2] + k_{35}[\text{H}_2\text{O}] + k_{36}[\text{e}]$
a12	NaCO ₂ ⁺	$k_{30}[\text{a}_{10}][\text{CO}_2][\text{M}] + k_{35}[\text{a}_{11}][\text{CO}_2]$	$k_{36}[\text{e}]$
a13	NaO ⁺	$k_{31}[\text{a}_{11}][\text{O}]$	$k_{32}[\text{N}_2] + k_{33}[\text{O}] + k_{34}[\text{O}_2] + k_{36}[\text{e}]$
a14	NaH ₂ O ⁺	$k_{35}[\text{a}_{11}][\text{H}_2\text{O}]$	$k_{36}[\text{e}]$

164

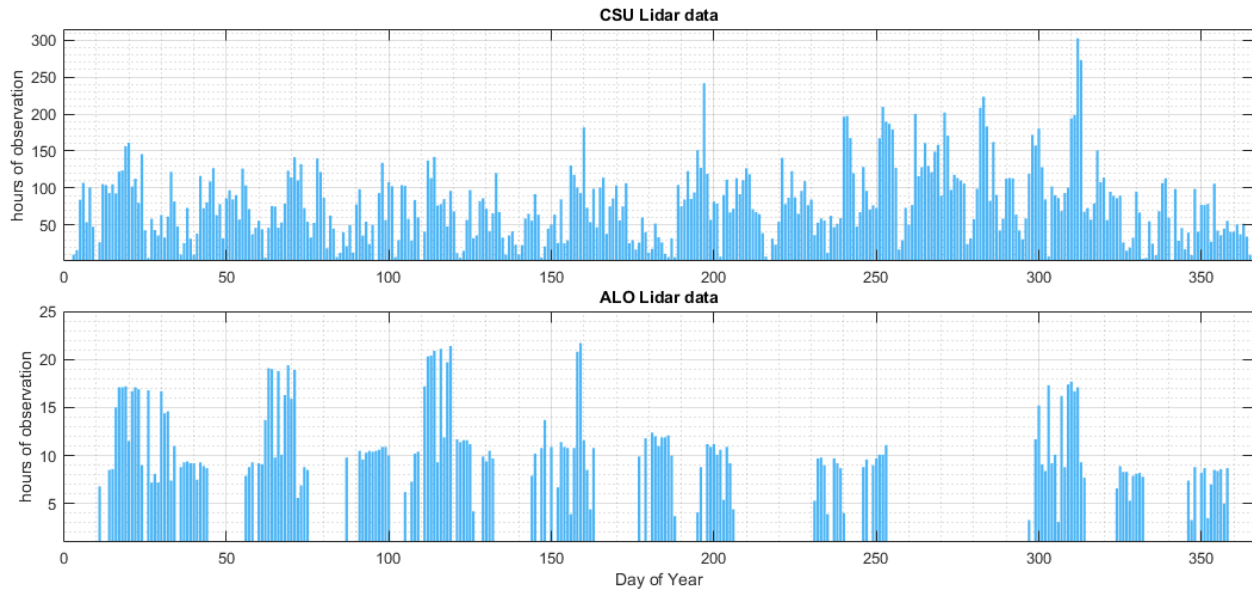
165 *In Species 1, as of the current state of the model, all Na(2p) atoms return to their ground state
166 immediately, so the loss term is set to 1. The [hν] is the term that represents loss via photon emission,
167 which follows a sinusoidal function based on the zenith angle of the respective local time.

168

169 3. CSU and ALO Sodium Lidar Observations and data processing

170 3.1 Observations

171 Several aspects of the current research, i.e., the presence of sodium in the MLT, require cross-validation
172 with the measurements. One primary objective of the present model is to match the observed seasonal
173 variation of the sodium layer. Measurements by the Colorado State University (CSU, 41.4°N, 111.5°W)
174 Lidar, also known as Utah State University (USU) Lidar, and the lidar data acquired by the Andes Lidar
175 Observatory (ALO, 30.3°S, 70.7°W), are used to facilitate the research in the current study. We are
176 unable to acquire more ALO data after 2019 as the COVID situation disrupted the site operation. The
177 CSU data comprises 27,930 hours of lidar observations between 1990 and 2020, whereas the ALO data
178 consists of 1872 hours between 2014 and 2019.



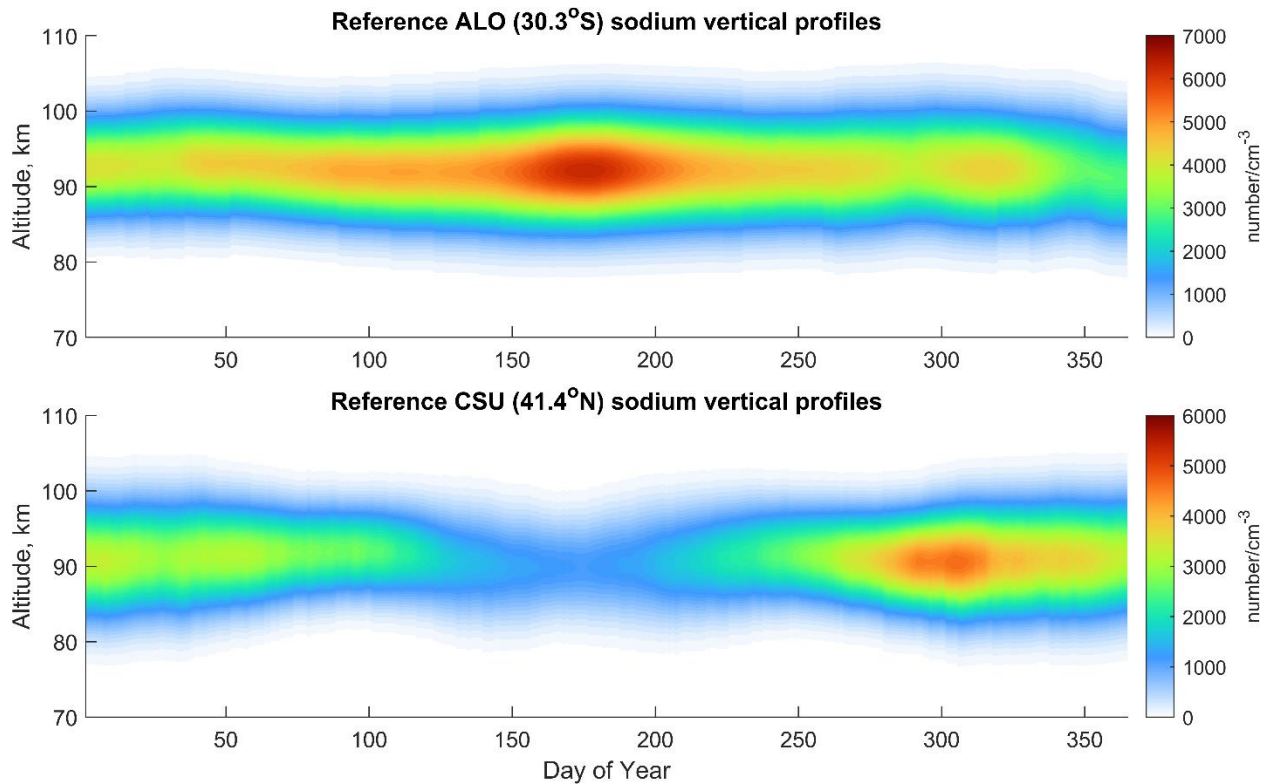
179

180 **Figure 1.** CSU lidar data from 1990 to 2020 (top plot) and ALO lidar data from 2014 to 2019 (bottom
 181 plot).

182 The statistics of CSU and ALO available data are presented in Figure 1. The Lidar observations of both
 183 sites consist of nocturnal observations only, and a typical nocturnal observation lasts between 8 and 11
 184 hours. Note that in Figure 1, there could be as many as 300 hours of sodium observations on a single day
 185 of year, which means the data of the date comprise observations of many years on that day in different
 186 years. The CSU data almost covered every day of the year with only a few exceptions, whereas the ALO
 187 data was much more sparse. As a result, due to the significantly larger number of CSU observations, the
 188 statistical reliability of the seasonal variation in the sodium layer derived from ALO observations may not
 189 be as strong as that of the CSU data. *As depicted in Figure 2, the overall seasonal trend of the sodium
 190 vertical profile derived from CSU lidar observations closely aligns with the simulation-based estimate by
 191 Marsh et al. (2013). In contrast, the results of ALO lidar observations diverge from the findings reported
 192 by Marsh et al. (2013).*

193 **3.2 Data processing**

194 The sodium layer in atmospheric observations is often affected by perturbations of atmospheric
 195 dynamics, which is why sodium is commonly used as a tracer in the study of the MLT dynamics (Plane et
 196 al., 2015). However, studying the sodium layer itself can be complicated due to the underlying chemical
 197 processes coupled with the dynamics. In order to mitigate the effects of atmospheric dynamics, we
 198 process the sodium vertical profiles from observations in three steps. First, we average the profiles by
 199 day of the year, meaning we take the average of the data from the same day of the year from different
 200 years. Missing data are treated using linear interpolation. Next, we smooth the averaged profiles using a
 201 15-day running average. Finally, we further smooth the profiles by fitting them with a skew-normal
 202 distribution (Azzalini & Valle, 1996) using the least squares error method.



203

204 **Figure 2.** The reference annual sodium vertical profiles at ALO (top plot) and at CSU (bottom plot). The
 205 reference profiles are the averages throughout all the available data on the same days at the respective
 206 site, then fitted by a *skew-normal* distribution that mitigates atmospheric dynamics. In essence, the
 207 reference profiles are measurements with small-scale dynamics removed via steps discussed in section
 208 3.2.

209

210 Figure 2 displays the processed annual sodium vertical profiles from the lidar measurements, referred to
 211 as reference profiles hereafter. These profiles serve as references to guide the numerical simulation of
 212 the NaChem model. The reference profiles are Na lidar measurements fitted using a skew-normal
 213 distribution, smoothed by a 15-day running average, and processed through linear 2-D interpolation
 214 across time and altitude. The lidar measurements have an altitude resolution of 500m for ALO and from
 215 75m to 140m for CSU. These measurements are interpolated to a 100m resolution as inputs to the
 216 NaChem model. The time resolution is interpolated to 0.1 seconds. The reference profiles inherently
 217 include diffusion and other dynamic effects on the sodium species in the MLT, as these observational
 218 data represent snapshots of sodium diffusion at various times. By constantly matching the observed Na
 219 profile to the simulated Na profile, the diffusion is included implicitly in the model. The seasonal column
 220 densities of both ALO and CSU profiles are similar to a sinusoidal function, with ALO data peaking near
 221 June and CSU data peaking in November. The centroid height of the sodium layer is higher in the ALO
 222 data than in the CSU data.

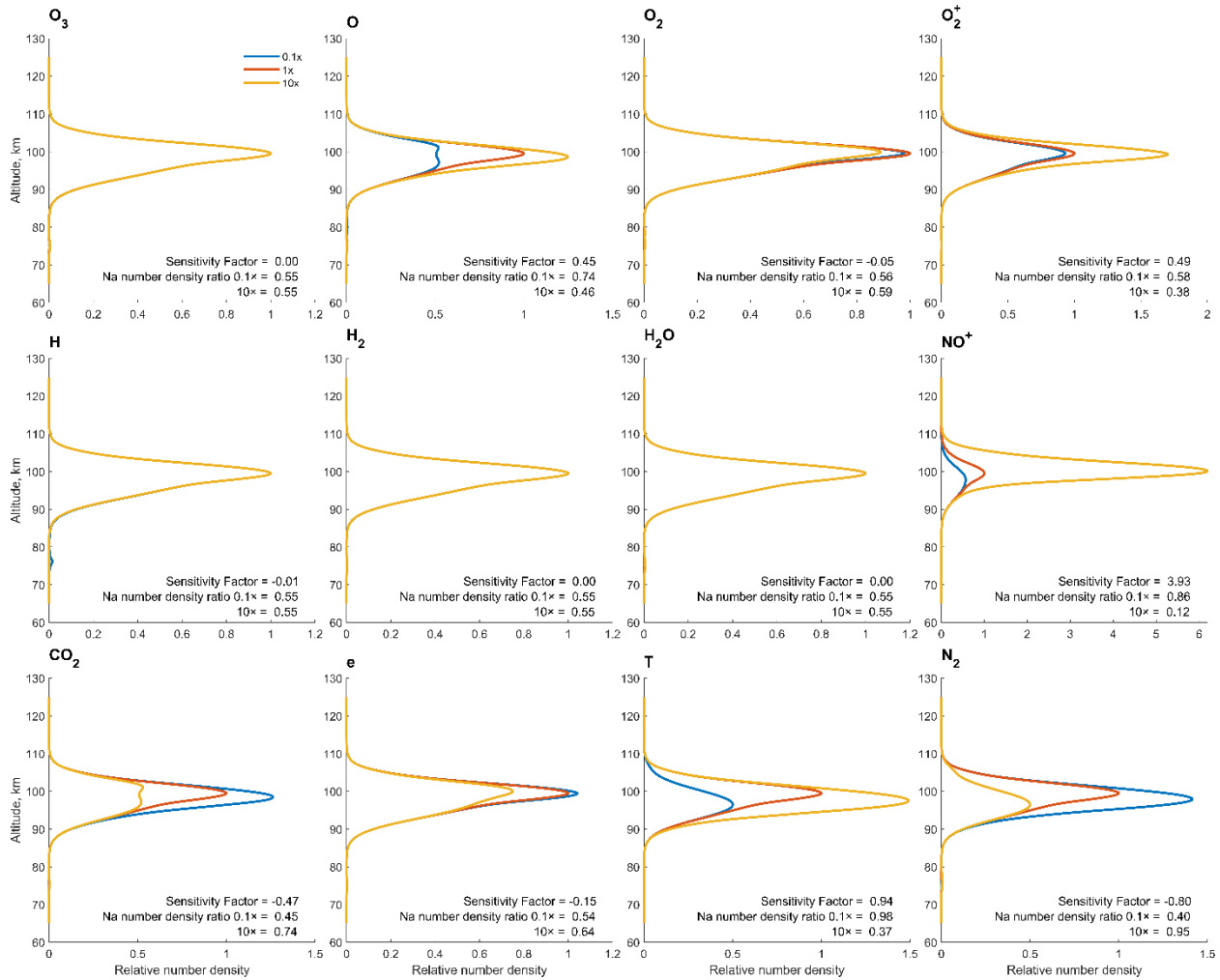
223

224 **4. Results**

225 4.1 Sensitivity test

226 Sodium in the atmosphere could manifest in many forms, i.e., in sodium-bearing neutral chemicals and
227 ionic chemicals. The sodium number densities are typically obtained via lidar measurements. Given the
228 complexity of the sodium chemistry, the observed sodium is merely a subset, possibly not even a major
229 constituent, of the total number of all the sodium-bearing species in the atmosphere. The total sodium
230 content is defined as the total number of sodium atoms in all 14 sodium-bearing species, as listed in
231 Table 2. In summary, the sodium that we can detect does not necessarily provide an accurate
232 representation of the total sodium content or the overall count of sodium-bearing species, as
233 unobservable species such as Na^+ and NaHCO_3 could constitute a substantial portion of the total sodium
234 content.

235 Understanding the impact of each background species, i.e., species listed in Figure 3., on the total
236 sodium content is essential to study the underlying mechanism of the chemical reactions. Therefore, we
237 present a sensitivity test by isolating variables. The sensitivity test is done by altering the number
238 density of background species in question by two orders of magnitude, i.e., with a factor of 0.1 and 10,
239 while keeping the number densities of other background species and the atomic sodium fixed. The
240 simulation is kept running until all the numbers are stable. The diurnal variations of the sodium and
241 background species are not considered in sensitivity test as they introduce unnecessary complexity. The
242 results of the sensitivity test of the 11 background species and temperatures involved in the numerical
243 simulation are shown in Figure 3. Each panel contains three lines, where the red curve shows the
244 unaltered vertical profile of the total sodium content. The results of the species altered by the factor of
245 0.1 and 10 are shown in light blue and yellow, respectively.



246

247 **Figure 3.** Sensitivity test of 11 background species and temperature on Na chemistry. The total sodium
 248 content vertical profile for the respective background species altered by 10x and 0.1x are shown in
 249 yellow and light blue. The reference sodium content vertical profiles are shown in red. Additionally, the
 250 sensitivity factor and the Na number density ratio to the concentration of all sodium species are
 251 presented on each panel.

252

253 In Figure 3, only the yellow curve is visible in some of the panels because the three curves are drawn on
 254 top of each other, indicating that the change of the respective background species bears little to no
 255 effect on the sodium chemistry. A sensitivity factor is defined to better quantify the weight of each
 256 background species in sodium chemistry. The factor is measured by the following equation:

257

$$\text{Sensitivity Factor} = \frac{NaT_c^{10} - NaT_c^{0.1}}{NaT_c} \quad (2)$$

258 Where NaT_c^{10} is the column density of the total sodium content with the respective species altered by a
 259 factor of 10, and $NaT_c^{0.1}$ is the same operation as the previous one but altered by a factor of 0.1. The
 260 denominator, NaT_c , is the column density of the reference profile. For example, a Sensitivity Factor of 5
 261 indicates that the total sodium content increases by five times when the respective background species

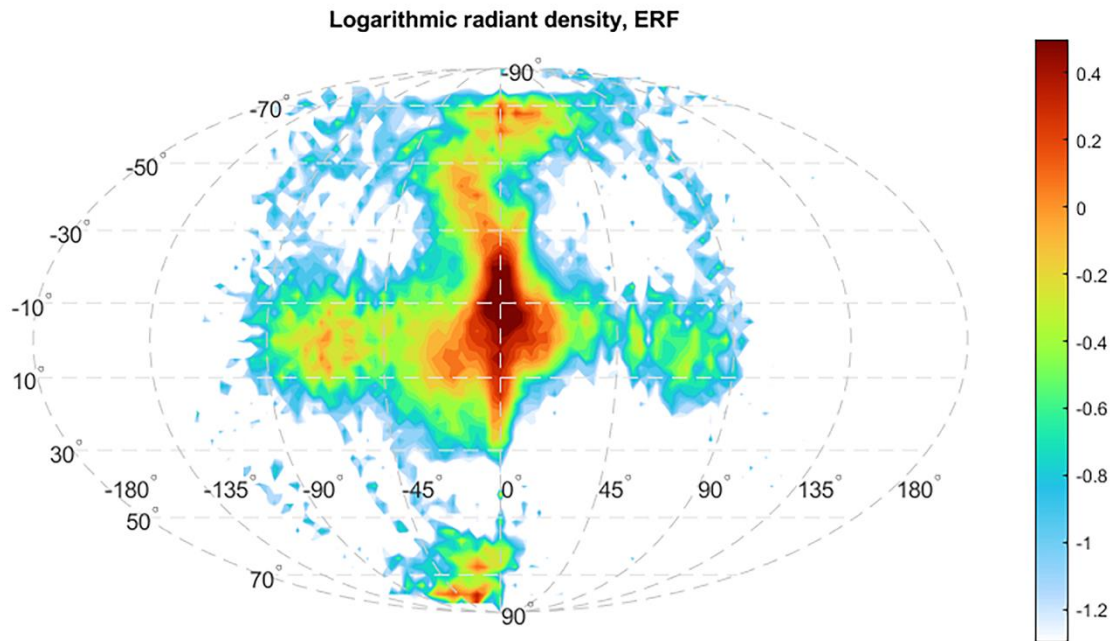
262 increases 100 times. A positive sensitivity factor indicates the total sodium content is positively
263 correlated to the respective species and vice versa. The reference profile is the total sodium content in
264 steady-state in the background condition of the midnight new year of 2002, giving a typical sodium
265 vertical profile similar to the one shown in Figure 5 of Plane (2004). In the simulation, a greater total
266 sodium content implies that a smaller percentage of the sodium chemicals are present as sodium atoms
267 as the altitude profile of the sodium atoms is fixed. In reality, instead of the sodium atoms, the total
268 sodium content should be more or less conserved. Hence a higher total sodium content in our
269 simulation suggests less sodium can be detected by the lidar.

270 Although the sensitivity factor could be different upon the change of the reference profile, it still gives
271 an insight into the significance of each background species to the sodium chemistry. Apparently, the
272 weight of some background species, namely O_3 , H, H_2 , and H_2O , is negligible in sodium chemistry,
273 meaning that removing these species and their associated reactions has no effect on the overall sodium
274 chemistry. Nevertheless, these species are still kept in our numerical model for completeness. The
275 impact of species that convert Na atom to Na^+ , as listed in reactions 27 and 28 of Table 1, is generally
276 strong. The effect of NO^+ , in particular, is the most significant according to the sensitivity factor, greater
277 than the combined effect of all the other species. Consequently, the number density of the sodium atom
278 by lidar observation is strongly correlated with the fluctuations of the NO^+ . In a nutshell, more NO^+ will
279 directly lead to fewer observable Na atoms. **That being said, the interaction between sodium and**
280 **background species is rather complex.** The scope of the **sensitivity factor** in the present paper was
281 limited to column density. As a result of such, variations and behaviors of the sodium chemicals by
282 altitude are overlooked. The actual impact of the background species may differ at different altitudes.

283 **4.2 Meteor input function**

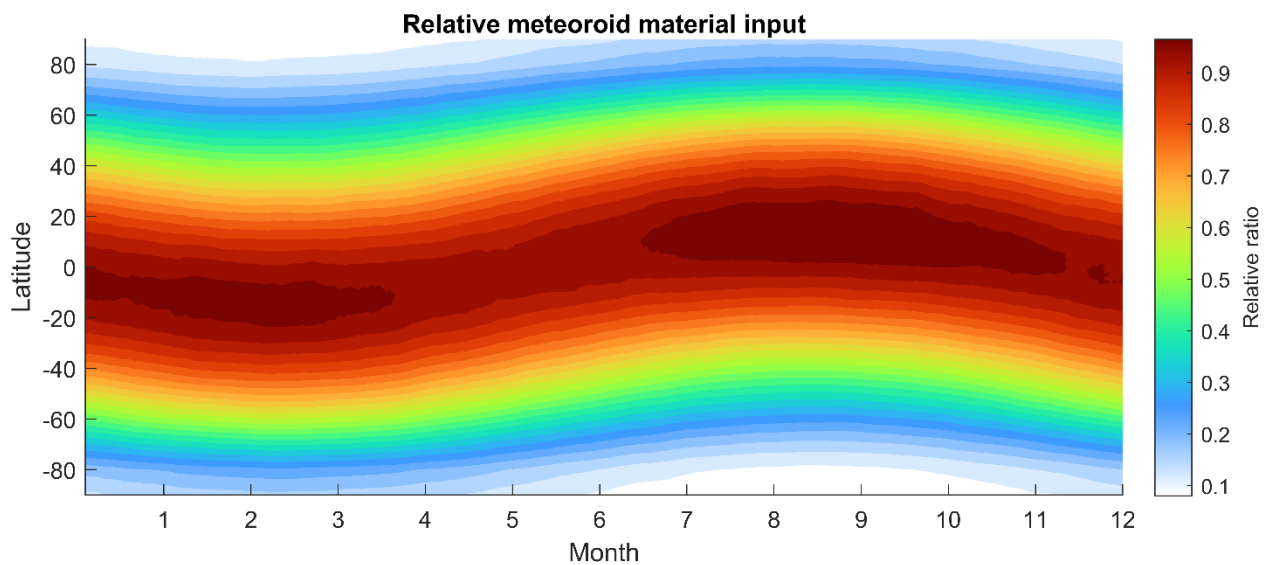
284 The estimation of meteoric influx is subject to many uncertainties among different techniques (Li et al.,
285 2022). Moreover, the meteor flux estimated by the sodium chemistry model also varies (Marsh et al.,
286 2014; Plane et al., 2015). The previous model of Plane (2004) and the following similar models indicate
287 that the rate of dimerization, or the speed of removing sodium from the system, is heavily correlated to
288 the vertical transport in the MLT. The NaChem model does not explicitly incorporate vertical transport,
289 but the vertical transport by diffusion is inherently embedded within the input of the observed sodium
290 vertical profile.

291 Unlike the previous models (Plane 2004; March et al. 2014; and references therein), the present
292 NaChem model took an indirect route to estimate the meteor mass input. **During the simulation, the**
293 **$NaHCO_3$ dimerization and the uptake of the sodium species on meteoric smoke particles, which can be**
294 **turned on or off, create a deficit of sodium atoms.** Meanwhile, a meteor input function injects an
295 appropriate amount of sodium atoms so that the present sodium vertical profile always matches the
296 reference profiles. This is carried out by finding the difference between the current sodium profile (with
297 the deficit) and the corresponding reference profile in every iteration and then replacing the former
298 with the latter. The diffusion coefficient is found to be highly correlated with the sink rate of the
299 dimerization reaction with large uncertainties (Plane, 2004). **The simulation circumvents this uncertainty**
300 **by directly incorporating the observational sodium vertical profile, given that diffusion is already**
301 **inherently in the measurements.**



302

303 **Figure 4.** Meteor radiant source derived from the AO observations. The result is in the Earth Reference
 304 Frame (ERF), equivalent to ground-based observations. The latitude of the ERF is centered on the ecliptic
 305 plane. The longitude of the ERF is centered to the Apex direction, the moving direction of the Earth,
 306 where the highest number of meteors encounter Earth.
 307 The radiant distribution is derived from the number of meteor events. Figure reproduced from Li et al. (2022).

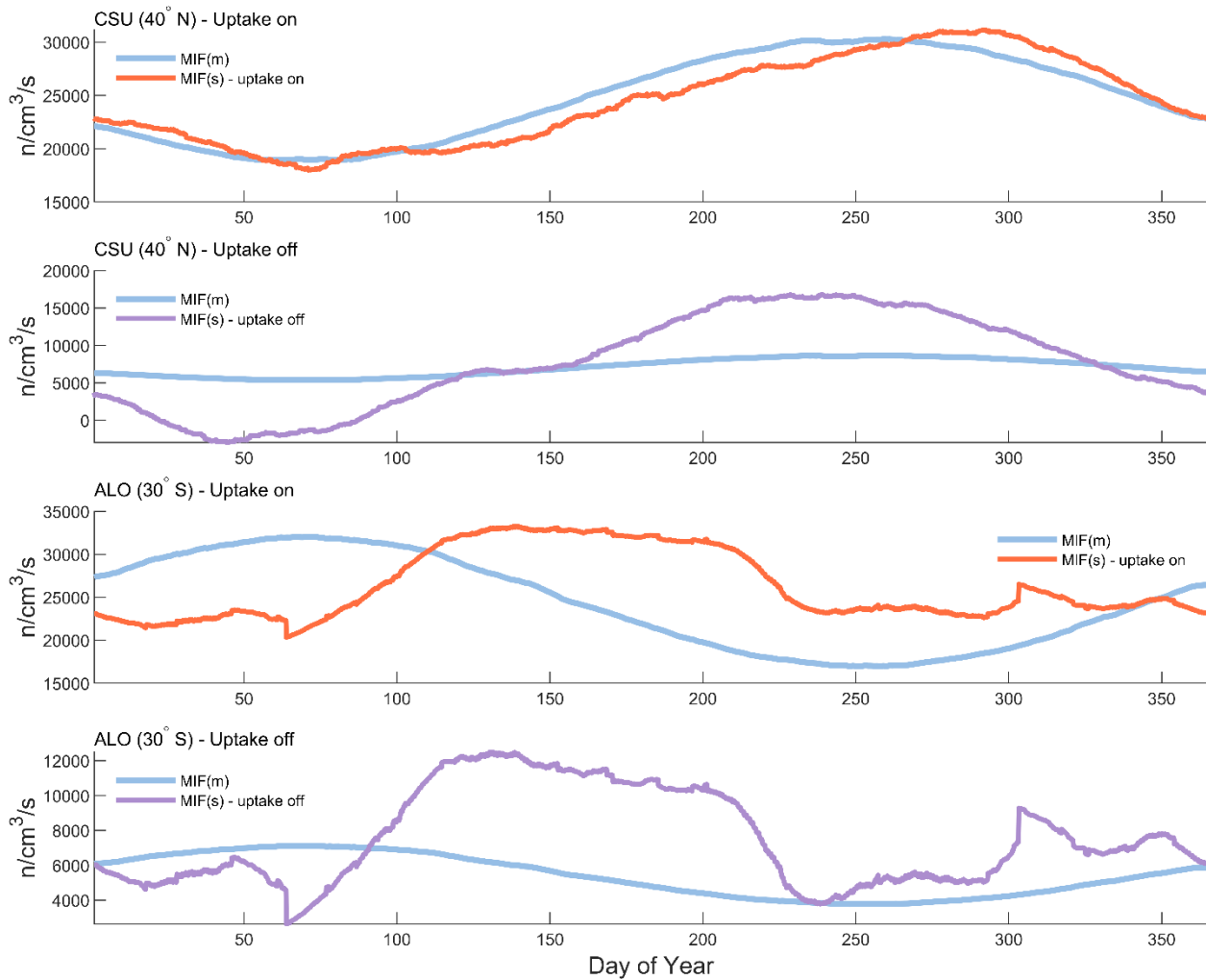


308

309 **Figure 5.** Relative seasonal and latitudinal meteoroid input, inferred from the radiant source distribution
 310 shown in Figure 4.

311

Sodium column injection rate



312

313 **Figure 6.** A comparison between two meteor input functions: MIF(m), which is inferred from micro-
 314 meteor radiant distribution, and MIF(s), which is derived using a Na chemistry model. The purple line
 315 represents MIF(s) with uptake on, while the orange dotted line represents MIF(s) with uptake off. The
 316 MIF(m) is linearly scaled to match each curve.

317

318 Figure 4 shows the high-resolution meteor radiant source distribution recently inferred from the AO
 319 observations (Li et al., 2022). The typical mass of the Arcibo meteors is estimated to be around 10^{-13} kg
 320 based on flux rate (Li and Zhou, 2019). Mathews et al. (2001) estimated the limiting meteor mass of 10^{-14}
 321 kg based on the meteor ballistic parameter. Limiting mass is the smallest mass a meteoroid must have
 322 to generate sufficient ionization to be detected by radar. Despite these estimations being based on
 323 various simplified assumptions that may lead to inaccurate results, the estimated mass is still at least
 324 two orders of magnitude smaller than the estimations of other facilities by similar means. More than
 325 95% of the meteoroid population in the Earth's atmosphere is found to be sporadic meteors by HPLA
 326 radar observation (Chau and Galindo, 2007), which typically are low-mass meteors evolved from the
 327 outer Solar system due to the Poynting-Robertson drag (Nesvorný et al., 2011; Koschny et al., 2019).

328 That being said, the percentage of sporadic meteors, as well as the radiant source distribution, are both
329 estimated based on the occurrence. However, the occurrence of sporadic meteors may not be able to
330 represent their mass distribution. The relative seasonal and latitudinal meteoroid input by the number
331 of **occurrences** inferred from the new radiant distribution is depicted in Figure 5. The meteoroid input
332 generally follows a sinusoidal pattern and differs from the one used in the previous work, as shown in
333 Figure 1 of Marsh et al. (2013). Although the interplanetary dust (meteor) background on the Earth's
334 orbit could vary in different locations due to a variety of reasons, e.g., Jupiter resonance, it is still safe to
335 assume no change in the interplanetary dust background for our purpose. Taking a stable interplanetary
336 dust background, the MIF(m) 's seasonal sinusoidal pattern should follow the Earth's axis rotation.

337 Figure 6 shows a comparison between two types of meteor input function: MIF(m), which is inferred
338 from the micro-meteor radiant distribution, and MIF(s), which is derived using the Na chemistry model
339 with sodium input from the lidar observations. For the MIF(s) model simulations, we did two scenarios,
340 one with and one without **uptake** by smoke particles, for the ALO and CSU data. The MIF(s) with uptake
341 by smoke particles exhibit a good match with the MIF(m) on the CSU dataset, while it does not show as
342 good of a match on the ALO dataset. The MIF(s) with smoke uptake on is represented by a purple line,
343 while the MIF(s) with smoke uptake turned off is depicted by an orange dotted line. The MIF(s) could go
344 negative when the reference sodium vertical profile decreases faster than the removal rate by the
345 dimerization, as shown in the orange dotted line in Figure 6, indicating that the dimerization process
346 alone is not sufficient enough to account for all the sodium atom depletion in the MLT region. MIF(m) is
347 derived from a global micro-meteor radiant distribution model, as depicted in Figure 4 and Figure 5. The
348 smoke uptake of sodium species in this study is implemented using a methodology similar to Plane
349 (2004), but instead of applying smoke uptake solely to the three major sodium species, namely Na,
350 NaHCO₃, and Na⁺, it is applied to all 14 sodium-bearing species. The optimal uptake factor to obtain the
351 best results was found to be 2×10^{-2} /km/s. The smoke uptake and NaHCO₃ dimerization account for
352 approximately 75% and 25% of the Na sink, respectively.

353 According to the global meteoroid orbital model outlined in Li et al., (2022), the latitudes spanning 29.5°
354 S to 30.5° S (ALO) account for 0.52% of the total meteor input, while those between 39.5° N and 40.5° N
355 (CSU) represent 0.67%. The CSU site shares more meteor input due to its closer proximity to one of the
356 Apex meteor radiant sources. The global total sodium injection rate inferred from the ALO data-based
357 simulation is 2.01×10^{23} atoms per second, and the CSU-data-based simulation suggests a global sodium
358 injection rate of 1.28×10^{23} atoms per second. Assuming the relative sodium elemental abundance in
359 meteoroid material is 0.8% (Vondrak et al., 2008), the deduced total meteoroid material input of ALO-
360 based simulation was 83 t d⁻¹. From CSU-based simulation, the rate is 53 t d⁻¹. Both estimations are close
361 to 80-130 t d⁻¹, the value reported by the Long Duration Exposure Facility (Love and Brownlee, 1993;
362 McBride et al., 1999). It is worth noting that the estimated total daily input of meteoroid materials
363 varies among previous studies, ranging from 4.6 t d⁻¹ (Marsh et al., 2013) to 300 t d⁻¹ (Nesvorný et al.,
364 2009), with an intermediate value of 20 t d⁻¹ reported by Carrillo-Sánchez et al. (2020). While these
365 estimates seem quite disparate, the variance is relatively small given that the daily input rate is derived
366 from combinations of chemicals that can fluctuate by several orders of magnitude. For example, the
367 NO⁺, which exhibits the highest sensitivity factor according to the sensitivity test, undergoes diurnal
368 variations of approximately three orders of magnitudes.

369

370 5. Discussion

371 The sodium concentration in the sodium layer in the MLT region is governed by several factors, including
372 chemistry, dynamics, and the MIF. It's difficult to discern which of these three components is more
373 important than the others. In this section, we discuss various factors that may contribute to modeling
374 the sodium concentration in the MLT.

375 The mass of the meteoroids has been estimated and measured using various methods. These include
376 the ballistic parameter derived from meteor deceleration (Mathews et al., 2001), estimation of meteor
377 head echo plasma distribution through a combination of meteor ablation models and radar cross-
378 section measurements (Close et al., 2005; Sugar et al., 2021), flux rate determination (Zhou and Kelley,
379 1997), as well as spacecraft in-situ measurements (Leinert and Grun, 1990), among others. The mass
380 estimated by the meteor ballistic parameter is commonly referred to as momentum or dynamical mass.
381 The mass estimated by the meteor ablation model is usually called the scattering mass. The meteor
382 momentum mass from Arecibo Ultra-High-Frequency (UHF) radar observation is estimated to be $10^{-14} -$
383 10^{-7} kg, with the typical mass being 10^{-13} kg. On the other hand, the meteor scattering mass is estimated
384 to be $10^{-9} - 10^{-5.5}$ kg by data from EISCAT UHF radar (Kero et al., 2008) and $10^{-7} - 10^{-4.5}$ kg by data from
385 ALTAIR UHF radar (Close et al., 2005). While the detection sensitivity among different facilities differs,
386 these estimations are still off by many orders of magnitude. The assessments of either momentum mass
387 or scattering mass are based on a variety of simplified assumptions. They are subject to errors due to
388 the complexity of radar beam patterns, background atmosphere conditions, aspect sensitivity, meteor
389 radiant sources, and many other possible factors. For example, radar meteor observation is subject to
390 bias against low-mass, low-velocity meteors (Close et al., 2007; Janches et al., 2015).

391 Another aspect that may contribute to the MIF(m)'s uncertainty is the meteor radiant distribution. The
392 meteor radiant distributions shown in Figure 4 and many others (Chau et al., 2004; Campbell-Brown and
393 Jones, 2006; Kero et al., 2012) are inferred or measured by meteor occurrence instead of mass input.
394 Currently, retrieving a more accurate estimation of the meteor mass input is still a topic under active
395 research, and there is no quantitative study on the disparities between meteor occurrence and meteor
396 mass input. The radiant sources of the meteors are expected to differ by mass as their orbital evolution
397 is highly correlated to their mass. The interplanetary dust interacts with the solar wind while in the Solar
398 System, losing its momentum in the process and evolving into orbits with a smaller semi-major axis and
399 lower eccentricity. The effect is called the Poynting-Robertson effect (Robertson and Russell, 1937),
400 which behaves like a drag force and defines the evolution of interplanetary dust, and it could be the
401 major reason for the existence of sporadic meteors (Li and Zhou, 2019; Koschny et al., 2019). The
402 importance of the Poynting-Robertson effect is highly dependent on the density and mass of the object.
403 By and large, the orbits of the smaller particles evolve exponentially faster. The orbital dynamics of
404 interplanetary particles have been very well summarized in section 2.2 of (Koschny et al., 2019). For the
405 reasons above, the meteor radiant distribution of mass could deviate from the radiant distribution of
406 occurrence. Therefore, the meteor input rates as shown in the blue curves of Figure 6 could be different
407 from those derived from the meteor radiant distribution of mass since they were derived from the
408 meteor radiant distribution by occurrence.

409 In the sodium chemistry model presented in this work, the MIF is the sole source of sodium, while the
410 sodium sink comprises NaHCO_3 dimerization and smoke uptake. The MIF(s) is determined by matching
411 the sink rate of the sodium atoms with the rate of sodium injection. In other words, MIF(s) represents

412 the amount of sodium injection needed to keep the sodium concentration equal to the reference
413 sodium profiles. If the chemical lifetime of sodium in the MLT is short, then the seasonal variation of
414 both the MIF and sodium concentration in the MLT should be similar. After examining Figures 3, 5, and
415 6, it can be observed that the averaged seasonal variation of sodium over the years at both sites (ALO
416 and CSU) does not correspond to the trend of the MIF(m) at their respective latitudes. This may indicate
417 that the chemical lifetime of sodium in the MLT should be relatively long, as there is no immediate effect
418 of MIF(m) on the sodium concentration. The MIF displays a sinusoidal pattern which peaks in March at
419 the ALO's latitude and in August at the CSU's latitude, whereas the sodium layer shows dual peaks in the
420 CSU's lidar observations and one peak in June in the ALO's lidar observations.

421 In this study, the MIF(s) derived from the NaChem simulation, based on the CSU lidar measurements
422 with uptake turned on, was able to match the amplitude of MIF(m) obtained from the meteor radiant
423 distribution. Although the model does not directly incorporate any dynamical processes, the vertical
424 transport by diffusion is implicitly included. The model forces the sodium layer to be the same as the
425 data, which are averaged by the observations of many years, in which the diffusions are inherently
426 embedded. The combination of observational data with the numerical chemistry model in this paper is a
427 relatively straightforward application of data assimilation (Bouttier & Courtier 2002). The lidar data of
428 both sites (CSU and ALO) indicate that the sodium column density consistently increases by about 20%
429 from 22:00 to 4:00 LT the next day. This can be attributed to the fact that, during nighttime, the large
430 deposits of Na^+ formed by daytime reactions slowly neutralized to Na. As a result, the sodium column
431 density consistently increases throughout the night. The same effect can be reproduced in the NaChem
432 simulation, albeit with a smaller amplitude. The simulation shows the increase to be about 8%. The
433 value is obtained by maintaining a constant total number of sodium-bearing species through the
434 deactivation of the sodium sink.

435 While meridional transport or atmospheric dynamics both contribute to the seasonal variation of the
436 sodium layer in the MLT, the diurnal sodium profile is the mean of observations of thousands of days, of
437 which the variation by atmospheric dynamics should be much less prominent. The lack of explicit
438 dynamics in the model may be one of the sources of inconsistency when compared to the observations.
439 Further, the WACCM, which supplied the background species to the NaChem, is an older version that
440 does not fully incorporate the dynamics of each ion species. Despite our results showing good
441 agreement between the MIF(s) and the MIF(m), there might be several plausible factors that could lead
442 to potential errors. For example, the Na sink by NaHCO_3 dimerization varies by the diffusion rate or the
443 vertical transport of sodium atoms in the chemistry model (Plane, 2004). Likewise, the MIF(m) may also
444 differ if the meteoroid mass input differs from the radiant source distribution by the occurrence of
445 meteors, as discussed in the aforementioned paragraph.

446 5. Conclusion

447 This work introduced a new sodium chemistry model that simulates the time evolution of all sodium-
448 bearing species using the continuity equation without making any steady-state assumption. The model
449 employs an exponential integrator and runs in high-time resolution to maintain numerical stability. The
450 model is simple to maintain in such a configuration and can be scaled up to include additional
451 capabilities more easily. The model is highly optimized for processing efficiency and benefits from the
452 use of an exponential integrator. Therefore, within an acceptable total CPU time, the NaChem can afford
453 a time resolution of up to milliseconds, several orders of magnitude smaller than those used in other Na

454 models. During our testing, the CPU time to simulated real-time ratio is about 1 to 1000 using a 0.1
455 second time step.

456 The model simulation was able to reproduce the seasonal variation of the sodium layer in the MLT by
457 simulations of chemical reactions. The simulation results at the CSU's latitude capture the general trend
458 of the seasonal variation at the location. The MIF(s) based on the ALO data exhibited less conformity
459 with the corresponding MIF(m), which could be attributed to inadequate statistics of the observational
460 data. Comparably, the CSU dataset is more reliable as the insufficient lidar hours in the ALO dataset may
461 lead to inaccurate statistics. In the simulation, when forcing the sodium layer to be the observation-
462 based reference profile, the inferred MIF is estimated to be 83 t d⁻¹ at ALO and 53 t d⁻¹ at CSU. The
463 numerical simulation by NaChem could reproduce the general trend of diurnal and seasonal variation of
464 the sodium layer compared to the observations by the CSU Lidar. There are some inconsistencies in
465 MIF(m) and MIF(s) based on data obtained from ALO Lidar. These inconsistencies may have originated
466 from poor statistics resulting from insufficient observation hours.

467 In summary, a new sodium chemistry model has been developed in this work to investigate the
468 relationship between MIF and the sodium layer. We also compared the MIF(m) derived from radar
469 meteor observation to the MIF(s) derived from the chemistry model and lidar observations. Our results
470 indicate that the uptake of sodium species onto meteoric smoke particles removes approximately three
471 times more sodium than the dimerization of NaHCO₃. Our future work will focus on incorporating the
472 plausible factors that may lead to potential errors discussed above into the chemistry model.

473

474

475 Acknowledgment

476 The study is supported by NSF Grant AGS-1903346. T.-Y. Huang acknowledges that her work is supported
477 by (while serving at) the National Science Foundation. WF was supported by the UK Natural Environment
478 Research Council (grant no. NE/P001815/1). Any opinions, findings, and conclusions or recommendations
479 expressed in this material are those of the authors and do not necessarily reflect the views of the National
480 Science Foundation. The lidar data used in this paper are obtained from The Utah State University (USU)
481 Sodium LIDAR facility and the Andes Lidar Observatory.

482

483 Code/Data availability

484 The CSU lidar data is available through Utah State University data service (Yuan, 2023). The ALO data is
485 available through the ALO online database (ALO, 2023). The WACCM data used in this work are available
486 through Penn State Scholarsphere (Li, 2023b).

487

488 Author contribution

489 Conceptualization, Yanlin L., Tai-Yin H. and Julio U.; methodology, Yanlin L.; software, Yanlin L.;
490 validation, Yanlin L., Tai-Yin H., Fabio V., Julio U. and Wuhu F.; formal analysis, Yanlin L., Tai-Yin H. and
491 Julio U.; investigation, Yanlin L., Tai-Yin H., Julio U. and Wuhu F.; resources, Tai-Yin H., Julio U., Fabio V.,
492 and Wuhu F.; data curation, Yanlin L.; writing---original draft preparation, Yanlin L.; writing---review and

493 editing, Yanlin L., Tai-Yin H., Julio U., Fabio V., and Wuhu F.; visualization, Yanlin L.; supervision, Julio U.
494 and Tai-Yin H.; project administration, Julio U. and Tai-Yin H.; funding acquisition, Julio U. and Tai-Yin H.
495 All authors have read and agreed to the published version of the manuscript.

496

497 Competing interests

498 The authors declare no competing interests.

499

500 Reference

501 Andrioli, V.F., Xu, J., Batista, P.P., Pimenta, A.A., Resende, L.C.D.A., Savio, S., Fagundes, P.R., Yang, G.,
502 Jiao, J., Cheng, X. and Wang, C.: Nocturnal and seasonal variation of Na and K layers simultaneously
503 observed in the MLT Region at 23 S. *Journal of Geophysical Research: Space Physics*, 125,
504 p.e2019JA027164, 2020.

505 ALO, <http://lidar.erau.edu/data/nalidar/index.php>, Accessed: 01 September 2023, 2023.

506 Azzalini, A., and Valle, A. D.: The multivariate skew-normal distribution. *Biometrika*, 83(4), 715-726, 1996.

507 Bag, T., Sunil Krishna, M., & Singh, V.: Modeling of Na airglow emission and first results on the nocturnal
508 variation at midlatitude. *Journal of Geophysical Research: Space Physics*, 120, 10–945, 2015.

509 Bowman, M., Gibson, A., and Sandford, M.: Atmospheric sodium measured by a tuned laser radar.
510 *Nature*, 221, 456–457, 1969.

511 Bouttier, F., and Courtier, P.: Data assimilation concepts and methods March 1999. Meteorological
512 training course lecture series. ECMWF, 718, 59, 2002.

513 Cai, X., Yuan, T., Eccles, J. V., Pedatella, N., Xi, X., Ban, C., and Liu, A. Z.: A numerical investigation on the
514 variation of sodium ion and observed thermospheric sodium layer at Cerro Pachón, Chile during equinox.
515 *Journal of Geophysical Research: Space Physics*, 124, 10395–10414, 2019.

516 Cai, X., Yuan, T., Eccles, J. V., and Raizada, S.: Investigation on the distinct nocturnal secondary sodium
517 layer behavior above 95 km in winter and summer over Logan, UT (41.7°N, 112°W) and Arecibo
518 Observatory, PR (18.3°N, 67°W). *Journal of Geophysical Research: Space Physics*, 124 (11), 9610–9625.
519 2019.

520 Campbell-Brown, M.: High resolution radiant distribution and orbits of sporadic radar meteoroids.
521 *Icarus*, 196, 144–163, 2008.

522 Campbell-Brown, M., and Jones, J.: Annual variation of sporadic radar meteor rates. *Monthly Notices of*
523 *the Royal Astronomical Society*, 367, 709–716, 2006.

524 Carrillo-Sánchez, J. D., Bones, D. L., Douglas, K. M., Flynn, G. J., Wirrick, S., Fegley Jr, B., and Plane, J. M.:
525 Injection of meteoric phosphorus into planetary atmospheres. *Planetary and Space Science*, 187,
526 104926, 2020.

527 Chau, J. L., and Galindo, F.: First definitive observations of meteor shower particles using a high-power
528 large-aperture radar. *Icarus*, 194, 23–29, 2008.

529 Chau, J. L., Woodman, R. F., and Galindo, F. (2007). Sporadic meteor sources as observed by the
530 Jicamarca high-power large-aperture vhf radar. *Icarus*, 188, 162–174.

531 Close, S., Brown, P., Campbell-Brown, M., Oppenheim, M., and Colestock, P.: Meteor head echo radar
532 data: Mass–velocity selection effects. *Icarus*, 186, 547–556, 2007.

533 Close, S., Oppenheim, M., Durand, D., and Dyrud, L.: A new method for determining meteoroid mass
534 from head echo data. *Journal of Geophysical Research: Space Physics*, 110, 2005.

535 Dunker, T., Hoppe, U.-P., Feng, W., Plane, J. M., and Marsh, D. R.: Mesospheric temperatures and
536 sodium properties measured with the alomar na lidar compared with waccm. *Journal of Atmospheric
537 and Solar-Terrestrial Physics*, 127, 111–119, 2015.

538 Feng, W., Marsh, D. R., Chipperfield, M. P., Janches, D., Hoffner, J., Yi, F., and Plane, J. M.: A global
539 atmospheric model of meteoric iron. *Journal of Geophysical Research: Atmospheres*, 118, 9456–9474,
540 2013.

541 Griffin, J., Worsnop, D., Brown, R., Kolb, C., and Herschbach, D.: Chemical kinetics of the $\text{NaO}(\text{a } 2\sigma^+) + \text{O}$
542 $(3p)$ reaction (Vol. 105) (No. 9). ACS Publications, 2001.

543 Gettelman, A., Mills, M. J., Kinnison, D. E., Garcia, R. R., Smith, A. K., Marsh, D. R., ... and Randel, W. J.:
544 The whole atmosphere community climate model version 6 (WACCM6). *Journal of Geophysical
545 Research: Atmospheres*, 124, 12380-12403, 2019.

546 Hedges, T., Lee, N., and Elschot, S.: Meteor Head Echo Analyses From Concurrent Radar Observations at
547 AMISR Resolute Bay, Jicamarca, and Millstone Hill. *Journal of Geophysical Research: Space Physics*, 127,
548 e2022JA030709, 2022.

549 Hedin, J., and Gumbel, J.: The global mesospheric sodium layer observed by odin/osiris in 2004–2009.
550 *Journal of atmospheric and solar-terrestrial physics*, 73, 2221–2227, 2011.

551 Higham, N. J.: Accuracy and stability of numerical algorithms. SIAM, 2002.

552 Hochbruck, M., and Ostermann, A.: Exponential integrators. *Acta Numerica*, 19, 209–286, 2010.

553 Huang, T.-Y., and Hickey, M. P.: Secular variations of OH nightglow emission and of the OH intensity-
554 weighted temperature induced by gravity-wave forcing in the MLT region. *Advances in Space Research*,
555 doi:10.1016/j.asr.2007.10.020, 2008.

556 Huang, T.-Y. and George, R.: Simulations of Gravity Wave-induced Variations of the OH(8,3), O₂(0,1), and
557 O(1S) Airglow Emissions in the MLT Region, *J. Geophys. Res. Space Physics*, 119,
558 doi:10.1002/2013JA019296, 2014.

559 Huang, T.-Y.: Gravity waves-induced airglow temperature variations, phase relationships, and krassovsky
560 ratio for oh (8, 3) airglow, o₂ (0, 1) atmospheric band, and o (1s) greenline in the mlt region. *Journal of
561 Atmospheric and Solar-Terrestrial Physics*, 130, 68–74, 2015.

562 Hunten, D. M.: Spectroscopic studies of the twilight airglow. *Space Science Reviews*, 6 (4), 493–573.
563 1967.

564 Hunten, D. M., Turco, R. P., and Toon, O. B.: Smoke and dust particles of meteoric origin in the
565 mesosphere and stratosphere. *Journal of Atmospheric Sciences*, 37(6), 1342-1357, 1980.

566 Hunziker, H. E., and Wendt, H. R.: Near infrared absorption spectrum of HO₂. *The Journal of Chemical*
567 *Physics*, 60, 4622-4623, 1974.

568 Janches, D., Swarnalingam, N., Plane, J., Nesvorny, D., Feng, W., Vokrouhlicky, D., and Nicolls, M.: Radar
569 detectability studies of slow and small zodiacal dust cloud particles. ii. a study of three radars with
570 different sensitivity. *The Astrophysical Journal*, 807, 13, 2015.

571 Kalashnikova, O., Horanyi, M., Thomas, G. E., and Toon, O. B.: Meteoric smoke production in the
572 atmosphere. *Geophysical research letters*, 27(20), 3293-3296, 2000.

573 Kero, J., Szasz, C., Nakamura, T., Meisel, D.D., Ueda, M., Fujiwara, Y., Terasawa, T., Nishimura, K. and
574 Watanabe, J.: The 2009–2010 MU radar head echo observation programme for sporadic and shower
575 meteors: radiant densities and diurnal rates. *Monthly Notices of the Royal Astronomical Society*, 425(1),
576 pp.135-146, 2012.

577 Kero, J., Szasz, C., Pellinen-Wannberg, A., Wannberg, G., Westman, A., and Meisel, D.: Three-
578 dimensional radar observation of a submillimeter meteoroid fragmentation. *Geophysical Research*
579 *Letters*, 35, 2008.

580 Koch, J., Bourassa, A., Lloyd, N., Roth, C., She, C.-Y., Yuan, T., and von Savigny, C.: Retrieval of
581 mesospheric sodium from osiris nightglow measurements and comparison to ground-based lidar
582 measurements. *Journal of Atmospheric and Solar-Terrestrial Physics*, 216, 105556, 2021.

583 Koch, J., Bourassa, A., Lloyd, N., Roth, C., and von Savigny, C.: Comparison of mesospheric sodium profile
584 retrievals from OSIRIS and SCIAMACHY nightglow measurements, *Atmos. Chem. Phys.*, 22, 3191–3202,
585 doi.org/10.5194/acp-22-3191-2022, 2022.

586 Koschny, D., Soja, R.H., Engrand, C., Flynn, G.J., Lasue, J., Lvasseur-Regourd, A.C., Malaspina, D.,
587 Nakamura, T., Poppe, A.R., Sterken, V.J. and Trigo-Rodríguez, J.M.: Interplanetary dust, meteoroids,
588 meteors and meteorites. *Space science reviews*, 215, pp.1-62, 2019.

589 Langowski, M.P., von Savigny, C., Burrows, J.P., Fussen, D., Dawkins, E., Feng, W., Plane, J. and Marsh,
590 D.R.: Comparison of global datasets of sodium densities in the mesosphere and lower thermosphere
591 from GOMOS, SCIAMACHY and OSIRIS measurements and WACCM model simulations from 2008 to
592 2012. *Atmospheric Measurement Techniques*, 10(8), pp.2989-3006, 2017.

593 Leinert, C., and Grün, E.: Interplanetary dust. *Physics of the inner heliosphere*, 207–275. Springer, 1990.

594 Li, J., Williams, B. P., Alspach, J. H., and Collins, R. L.: Sodium resonance wind-temperature lidar at pfr:
595 Initial observations and performance. *Atmosphere*, 11, 98, 2020.

596 Li, Y., and Zhou, Q.: Velocity and orbital characteristics of micrometeors observed by the arecibo 430
597 mhz incoherent scatter radar. *Monthly Notices of the Royal Astronomical Society*, 486 (3), 3517–3523,
598 2019.

599 Li, Y., Zhou, Q., Scott, M., and Milla, M.: A study on meteor head echo using a probabilistic detection
600 model at jicamarca. *Journal of Geophysical Research: Space Physics*, 125 (1), e2019JA027459, 2020.

601 Li, Y., Zhou, Q., Urbina, J., and Huang T.-Y.: Sporadic micro-meteoroid source radiant distribution
602 inferred from the Arecibo 430 MHz radar observations, *Monthly Notices of the Royal Astronomical
603 Society*, 2022.

604 Li, Y., Galindo, F., Urbina, J., Zhou, Q. and Huang, T.Y.: A Machine Learning Algorithm to Detect and
605 Analyze Meteor Echoes Observed by the Jicamarca Radar. *Remote Sensing*, 15, p.4051, 2023a.

606 Li, Y. Scholarsphere, [https://scholarsphere.psu.edu/resources/b91f6404-71fd-4d0e-9adc-
607 9e42457b5703](https://scholarsphere.psu.edu/resources/b91f6404-71fd-4d0e-9adc-9e42457b5703), Accessed: 01 September 2023, 2023b.

608 Love, S., & Brownlee, D.: A direct measurement of the terrestrial mass accretion rate of cosmic dust.
609 *Science*, 262, 550–553, 1993.

610 Marsh, D. R., Janches, D., Feng, W., and Plane, J. M.: A global model of meteoric sodium. *Journal of
611 Geophysical Research: Atmospheres*, 118, 11–442, 2013.

612 Mathews, J., Janches, D., Meisel, D., and Zhou, Q.-H.: The micrometeoroid mass flux into the upper
613 atmosphere: Arecibo results and a comparison with prior estimates. *Geophysical Research Letters*, 28,
614 1929–1932, 2001.

615 McBride, N., Green, S. F., and McDonnell, J.: Meteoroids and small sized debris in low earth orbit and at
616 1 au: Results of recent modelling. *Advances in Space research*, 23 (1), 73–82, 1999.

617 Molod, A., Takacs, L., Suarez, M., and Bacmeister, J.: Development of the GEOS-5 atmospheric general
618 circulation model: Evolution from MERRA to MERRA2. *Geoscientific Model Development*, 8(5), 1339-
619 1356, 2015.

620 Nesvorný, D., Vokrouhlický, D., Pokorný, P., and Janches, D.: Dynamics of dust particles released from
621 Oort cloud comets and their contribution to radar meteors. *The Astrophysical Journal*, 743, 37, 2011.

622 Nesvorný, D., Jenniskens, P., Levison, H. F., Bottke, W. F., Vokrouhlický, D., and Gounelle, M.: Cometary
623 origin of the zodiacal cloud and carbonaceous micrometeorites. Implications for hot debris disks. *The
624 Astrophysical Journal*, 713, 816, 2010.

625 Pifko, S., Janches, D., Close, S., Sparks, J., Nakamura, T., and Nesvorný, D.: The Meteoroid Input Function
626 and predictions of mid-latitude meteor observations by the MU radar. *Icarus*, 223(1), 444-459, 2013.

627 Plane, J.: A time-resolved model of the mesospheric Na layer: constraints on the meteor input function.
628 *Atmospheric Chemistry and Physics*, 4, 627–638, 2004.

629 Plane, J., Oetjen, H., de Miranda, M., Saiz-Lopez, A., Gausa, M., and Williams, B.: On the sodium d line
630 emission in the terrestrial nightglow. *Journal of atmospheric and solar-terrestrial physics*, 74 , 181–188,
631 2012.

632 Plane, J.: A reference atmosphere for the atomic sodium layer. *Atmos. Chem. Phys*, 470, 2010.

633 Plane, J. M., Daly, S. M., Feng, W., Gerding, M., and Gómez Martín, J. C.: Meteor-ablated aluminum in
634 the mesosphere-lower thermosphere. *Journal of Geophysical Research: Space Physics*, 126,
635 e2020JA028792, 2021.

636 Plane, J. M., Feng, W., and Dawkins, E. C.: The mesosphere and metals: Chemistry and changes.
637 *Chemical reviews*, 115, 4497–4541, 2015.

638 Qiu, S., Wang, N., Soon, W., Lu, G., Jia, M., Wang, X., Xue, X., Li, T. and Dou, X.: The sporadic sodium
639 layer: a possible tracer for the conjunction between the upper and lower atmospheres. *Atmospheric*
640 *Chemistry and Physics*, 21, pp.11927-11940, 2021.

641 Robertson, H.: Dynamical effects of radiation in the solar system. *Monthly Notices of the Royal*
642 *Astronomical Society*, 97, 423, 1937.

643 Sugar, G., Marshall, R., Oppenheim, M., Dimant, Y., and Close, S.: Simulation-derived radar cross sections
644 of a new meteor head plasma distribution model. *Journal of Geophysical Research: Space Physics*, 126,
645 e2021JA029171, 2021.

646 Takahashi, T., Nozawa, S., Tsutsumi, M., Hall, C., Suzuki, S., Tsuda, T.T., Kawahara, T.D., Saito, N., Oyama,
647 S., Wada, S. and Kawabata, T.: October. A case study of gravity wave dissipation in the polar MLT region
648 using sodium LIDAR and radar data. *Annales Geophysicae*, Vol. 32, No. 10, pp. 1195-1205, 2014.

649 Vondrak, T., Plane, J., Broadley, S., and Janches, D.: A chemical model of meteoric ablation. *Atmospheric*
650 *Chemistry and Physics*, 8, 7015–7031, 2008.

651 Yuan, T., Usu-CSU NA LIDAR Data, DigitalCommons@USU. Available at:
652 https://digitalcommons.usu.edu/all_datasets/54/, Accessed: 01 September 2023, 2023

653 Yu, B., Xue, X., Scott, C.J., Jia, M., Feng, W., Plane, J., Marsh, D.R., Hedin, J., Gumbel, J. and Dou, X.:
654 Comparison of middle-and low-latitude sodium layer from a ground-based lidar network, the Odin
655 satellite, and WACCM–Na model. *Atmospheric Chemistry and Physics*, 22(17), pp.11485-11504, 2022.

656 Zhou, Q. H., and Kelley, M. C.: Meteor observations by the arecibo 430 mhz incoherent scatter radar. ii.
657 results from time-resolved observations. *Journal of Atmospheric and Solar-Terrestrial Physics*, 59 (7),
658 739–752.110, 1997.

659

660

661

662

663

664

665

666

667

668

669